Robust Fano resonance in the photonic valley Hall states

Chang-Yin Ji,[1,2] Yongyou Zhang,[1,*] Bingsuo Zou,[3] and Yugui Yao[1,†]

[1]*Key Lab of advanced optoelectronic quantum architecture and measurement (MOE), Beijing Key Lab of Nanophotonics & Ultrafine Optoelectronic Systems, and School of Physics, Beijing Institute of Technology, Beijing 100081, China*

[2]*China Academy of Engineering physics, Mianyang, Sichuan 621900, China*

[3]*Guangxi Key Laboratory of Processing for Non-ferrous Metals and Featured Materials, School of Physical science and Technology, Guangxi University, Nanning 530004, China*

(Received 17 July 2020; revised 19 September 2020; accepted 21 January 2021; published 11 February 2021)

Rapidly developing photonics brings many interesting resonant optical phenomena, in which the Fano resonance (FR) always intrigues researchers because of its applications in optical switching and sensing. However, its sensitive dependence on environmental conditions makes it hard to implement in experiments. In this work we suggest a robust FR based on the photonic valley Hall insulators, immune to the system impurities. The robust FR is achieved by coupling the valley-dependent edge states with one double-degenerate cavity. The δ-type photonic transport theory we build reveals that this FR dates from the interference of the two transmissions that are attributed to the two cavity modes. We confirm that the induced Fano line shape of the transmission spectra is robust against the bending domain walls and disorders. Our work may provoke exciting frontiers for manipulating the valley transport and pave a way for the valley photonic devices such as optical switches, low-threshold lasers, and ultrasensitive sensors.

DOI: 10.1103/PhysRevA.103.023512

I. INTRODUCTION

Since Haldane and Raghu transferred electronic topological phases to classical photonics [1], photonic topological insulators have triggered plenty of research interests [2–9]. They not only enriched the realm of photonics but also provided a promising research perspective for robustly manipulating photon transport against system impurities. Because the macroscopic optical meta-atoms can be easily engineered into various architectures, photonic metamaterials are an ideal platform for exploring and verifying the fascinating topological phases in electronic systems [10–14]. A number of optical analog topological phases have been realized theoretically and experimentally, such as quantum Hall effect (QHE) [15,16], quantum spin Hall effect (QSHE) [17–25], Weyl semimetals [26–34], high-order topological insulators [35–40], photonic topological valley Hall effect [41–53], and so on [54–57]. Topological quantum states can also be induced by spatially uniform optical excitations [58]. When active materials or sources [59] are introduced, the system could present a topological phase transition, for example, Chern topological sound wave in active-liquid metamaterials [60].

One remarkable application of the photonic topological insulators is the robust transport of the topological edge states (TESs), protected by the nontrivial topology of the systems. The robust transport has been widely studied in experiments and theories, while the effect of defect-based cavities on the robustness of the TESs is still far less considered [9,61,62]. For the optical analogues of Chern topological insulators, the chiral TESs are indeed unprecedented robustness, that is, the backscattering of the edge states is prohibited, for example, in an active system without the time reversal symmetry [60]. However, the TES transport may show fragility in the systems with the time reversal symmetry because a pair of time reversal modes can always be coupled together by a possible mechanism, for example, recent works on the QSHE in the photonic and acoustic topological insulators [61,62]. The breaking of the unidirectional transport provides the tunability for the transport of the TESs, possessing significant potential applications, such as switches. Unfortunately, the topological insulators in Ref. [61] not only require C_6 symmetry, but also are hard for designing a large matching gap between the two topologically-inequivalent insulators. Additionally, there is an inherent band gap at the time reversal invariant point in the TES dispersion, which indicates that the backscattering of the TES propagation is not totally immune around such a point. These characteristics are not favorable for potential applications. It is thus significant and urgent to find new topological systems to overcome them.

The photonic valley Hall insulators (PVHIs) which can be achieved by common dielectric materials provide a simple route for exploring the photonic valley edge states (VESs) in a wide range of the electromagnetic spectrum. Here, we show that PVHIs can serve as an ideal candidate to implement the manipulation of the VESs, simultaneously without the above shortcomings. We find that the defect cavities with frequency falling into the bulk band gap of the PVHIs can break the backscattering immunity of the VES propagation, leading to the perfect reflection [61]. Moreover, an ideal Fano resonance

*Author to whom correspondence should be addressed: yyzhang@bit.edu.cn

†ygyao@bit.edu.cn

(FR), i.e., valley transmission sharply changes from zero to one, is implemented by a degenerate cavity that is felicitously engineered to side couple with the VESs. The profile of this FR is robust against the bending domain wall and disorders. The tunability of the VES transport and its robustness against fabrication imperfection together enlarge the realm of applications of the photonic valley Hall insulators, because of high desire in many scenarios for designing topology-based devices [63–75].

The rest of the present work is organized as follows. In Sec. II, the PVHIs are designed and their topologies are confirmed by the band Berry curvatures. In Sec. III, the Fano line-shape transmission is first demonstrated by coupling the VESs with a degenerate cavity and the FR robustness is then numerically confirmed. In Sec. IV, a waveguide-cavity transport theory is build to demonstrate the underlying mechanism of the fascinating FR. At last, we arrive at a brief conclusion in Sec. V.

II. PHOTONIC VALLEY HALL INSULATORS

The designed PVHIs are the two-dimensional hexagonal lattices with an angle-cut triangle meta-atom embedded in the air background, see the unit cells A and B in Figs. 1(a) and 1(b). The asymmetry of the angle-cut triangle meta-atom is responsible for the phase transition. Such an asymmetry could also be obtained by using the anisotropic permittivity and permeability [76,77]. The long and short side lengths are set to be $l = 0.61a$ and $d = 0.1a$, respectively, where a is the lattice constant. For them the meta-atoms are composed of nonmagnetic material with the relative dielectric constant $\varepsilon_r = 16$ which can be achieved in the microwave and visible regions [78,79]. The magnetic and electric fields for the considered photonic topological states are perpendicular and parallel to the unit-cell plane, respectively. Since the triangle meta-atoms are rotated $\pm 30^\circ$ with respect to the horizontal lattice vector direction for the cells A and B in the Figs. 1(a) and 1(b), respectively, their six Dirac degeneracy points at the Brillouin zone (BZ) corners are both lifted up to form a global band gap between the second and third bands, essentially owing to the breaking of the system C_{3v} symmetry. The mutual mirror symmetry along the horizontal lattice vector between the unit cells A and B is responsible for the identity of the two bands in Figs. 1(a) and 1(b), but note that the two bands present different topology near the Brillouin zone (BZ) corners, referred to Figs. 1(c)–1(f).

The different topologies of the first two bands can be confirmed by analyzing the Berry curvature, defined as [80]

$$F_{\boldsymbol{k}}^{(n)} \equiv \nabla_{\boldsymbol{k}} \times \boldsymbol{A}_{\boldsymbol{k}}^{(n)}, \tag{1}$$

with the band index n, Bloch wave vector $\boldsymbol{k}$, and Berry connection $\boldsymbol{A}_{\boldsymbol{k}}^{(n)}$. The Berry connection has the following form:

$$\boldsymbol{A}_{\boldsymbol{k}}^{(n)} = \langle u_{\boldsymbol{k}}^{(n)} | \nabla_{\boldsymbol{k}} | u_{\boldsymbol{k}}^{(n)} \rangle, \tag{2}$$

where $|u_{\boldsymbol{k}}^{(n)}\rangle$ is the periodic part of the Bloch wave function in the system. It is more convenient to calculate the lattice field strength of $\widetilde{F}_{\boldsymbol{k}}^{(n)}$ rather than $F_{\boldsymbol{k}}^{(n)}$ [80]. As the discretized area of $d^2\boldsymbol{k}$ is small enough, one has $\widetilde{F}_{\boldsymbol{k}}^{(n)} \approx F_{\boldsymbol{k}}^{(n)} d^2\boldsymbol{k}$. The values

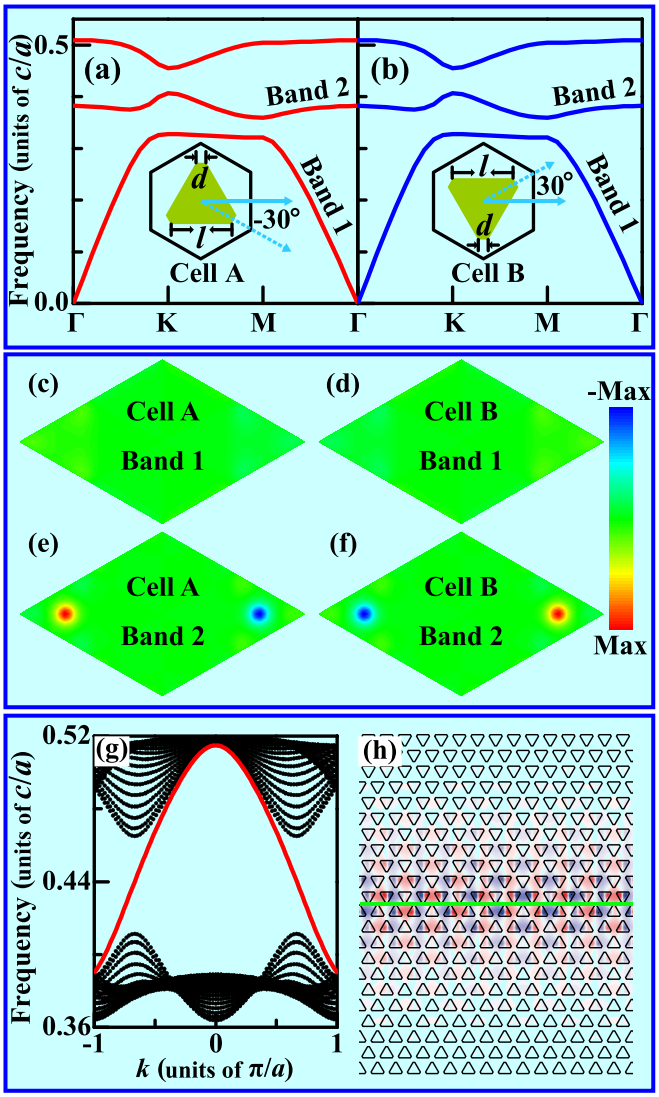

FIG. 1. (a, b) Band structures of two photonic topological valley Hall insulators. Their unit cells A and B are, respectively, given in the insets of panels (a) and (b), both composed of an angle-cut triangle meta-atom embedded in air. Their lattice periods are set to be a with $l = 0.61a$ and $d = 0.1a$. The triangular-like meta-atom is nonmagnetic material with relative dielectric constant $\varepsilon_r = 16$. (c–f) Distributions of lattice field strength in the first Brillouin zone. Panels (c) and (d) are those of bands 1 for cells A and B, while panels (e) and (f) are those of bands 2 for cells A and B. (g) One-dimensional photonic band diagram of the ribbon-shaped super cell in panel (h). The red and black curves are for the VESs and bulk states, respectively. (h) Magnetic field distribution of the VESs. The attenuated field tells that the VES is localized around the domain wall.

of $\widetilde{F}_{\boldsymbol{k}}^{(n)}$ for the bands 1 in Figs. 1(a) and 1(b) are shown in Figs. 1(c) and 1(d), respectively. The zero $\widetilde{F}_{\boldsymbol{k}}^{(n)}$ in the whole BZ tells that the bands 1 are trivial. On the contrary, the bands 2 in Figs. 1(a) and 1(b) have nonzero $\widetilde{F}_{\boldsymbol{k}}^{(n)}$ near the BZ corners, see Figs. 1(e) and 1(f), respectively. The nonzero $\widetilde{F}_{\boldsymbol{k}}^{(n)}$ implies the nontrivial topology of the bands 2. The time reversal symmetry is responsible for the zero sum of $\widetilde{F}_{\boldsymbol{k}}^{(n)}$ in the whole BZ. This nontrivial topology can be characterized

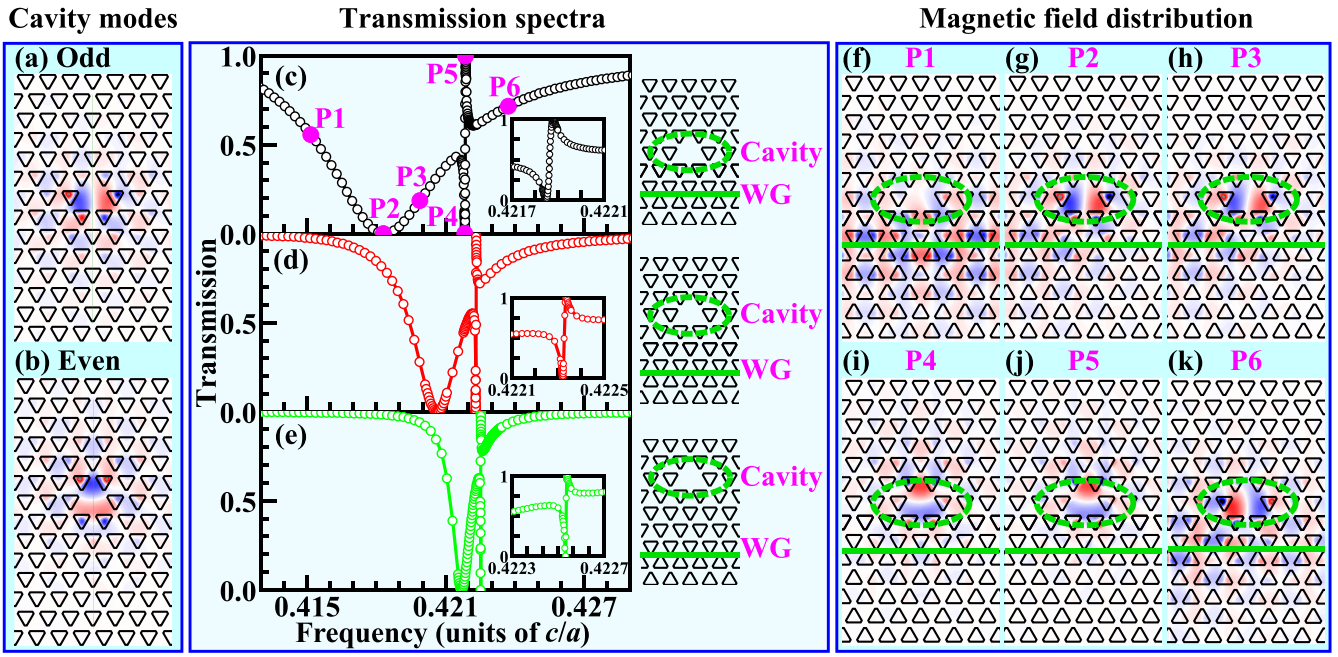

FIG. 2. (a, b) Field distributions of the two degenerate cavity modes with odd and even parities (along the horizontal direction), respectively. (c–e) Transmission spectra of the VESs coupled with the double-degenerate cavity calculated by the finite element method within the COMSOL code. The optical structures are adopted on the right side, whose distance between the cavity and the WG increases from two layers to four layers. The insets are the enlarged views of the Fano profiles and the solid lines are guides for eyes. (f–k) Field distributions whose frequencies of the incident light correspond to the magenta dots marked in panel (c). The positions of the domain walls and cavities are denoted by the green solid lines and dashed ellipses, respectively.

by the valley-dependent topological index, that is, the valley Chern number defined as $C_V \equiv C_{\boldsymbol{K}} - C_{\boldsymbol{K}'}$. The $C_{\boldsymbol{K}}$ ($C_{\boldsymbol{K}'}$) is the sum of $\widetilde{F}_{\boldsymbol{k}}^{(n)}$ around the $\boldsymbol{K}$ ($\boldsymbol{K}'$)-valley. Figures 1(e) and 1(f) show that the sign of $C_{\boldsymbol{K}}$ ($C_{\boldsymbol{K}'}$) for the band 2 in Fig. 1(a) is opposite with that for the band 2 in Fig. 1(b). Therefore, there is a nonzero C_V across the domain wall when it is formed by the PTVH insulators in Figs. 1(a) and 1(b).

Note that $|C_V|$ is in the range of (0, 1), in general not a well-defined integer [51]. This is attributed to the large band gap that overlaps the Berry curvatures at the $\boldsymbol{K}$ and $\boldsymbol{K}'$ valleys. However, the effective Hamiltonian within the $\boldsymbol{k}\cdot\boldsymbol{p}$ perturbation theory can give $|C_V| = 1$ [50]. The existence of the VESs does not require a well-defined integer valley Chern number, see the red curves in Fig. 1(g) which demonstrates the dispersion of the VESs with the band gap in the range of $(0.413,\ 0.463)\frac{c}{a}$. The VESs arise from a large distance separating $\boldsymbol{K}$ and $\boldsymbol{K}'$ valleys, leading to $C_V \neq 0$. Since the nonquantized C_V can be varied smoothly when the system is deformed, the VESs is not really protected in principle. Nevertheless, given the nonzero C_V, one needs to deform the system by quite a lot before the VESs are completely ruined. The VES dispersions in Fig. 1(g) correspond to the angle-to-angle interface in Fig. 1(h), which can be taken as an ideal waveguide (WG), denoted by the green solid line. Owing to $C_V \neq 0$, the VESs as the WG states are commonly immune to the structure imperfection. The color map displays an example of the field distribution of the VES. Note that the VESs can also be achieved in a square lattice [81]. This abundance of the architecture diversity benefits the application of the valley topological insulators. Moreover, another merit of the present system is that the rightward- and leftward-moving VESs are fully gapless, see Fig. 1(g), with respect to the optical analog of the QSHE in Ref. [61]. If the designed defect cavities can tune the transportation of the VESs, then the PVHIs would show widespread potential for the optical application, for example, the robust FR.

III. ROBUST FANO RESONANCE

For the topological phases in electronic systems, the propagation of the TESs is robust against the system imperfections, such as bending domain walls, defect cavities, disorders, and so on. As a rational conjecture, researchers instinctively believe that the propagation of all types of the TESs in photonics should be immune to the aforementioned imperfections. However, the defect cavities with frequencies in the topological band gap can significantly break the robust pseudospin-polarized transport of photonic TESs, because the introduced defect cavities inevitably violate the system crystal symmetries [61]. This property as a merit provides a powerful tool for tuning the propagation of the TESs in various photonic topological devices. Since the valley topology depends on the crystal symmetry, it can also be achieved in the valley systems. Back scatterings between leftward- and rightward-moving edge states are allowed by certain δ-types of cavities, providing the needed momentum. In Figs. 2(a) and 2(b), a double degenerate cavity is designed as an example to show the propagation tuning of the VESs. The cavity is formed by simply removing one photonic meta-atom. Since the cavity has the D_3 symmetry, it holds a pair of degenerate modes with

the odd and even parities, respectively, see the field distributions in Figs. 2(a) and 2(b). The eigenvalue analysis confirms that their frequencies are equal to $\sim 0.42269c/a$, being in the bulk band gap.

Let us focus on the strong interaction of such a type of degenerate cavities with the VESs in the following. When the cavity is side placed near the topological WG, it will influence the propagation of the VESs, see the transmission spectra in Figs. 2(c)–2(e) whose structures are shown on the right side. The transmission spectra are all obtained by the scattering matrix method [61,82]. The lattice for calculation should be large enough to prevent the modes from leaking into the air domain. Its size in this work is set to be $44a$ and $22\sqrt{3}a$ in horizontal and vertical directions, respectively. The D_3 symmetry of the cavity is broken by the presence of the WG and therefore, the degeneracy of the cavity modes is lifted up, reflected by the two zero transmission points in frequency. The two zero transmission points confirm that the propagation of the VESs is strongly disturbed near the cavity eigenfrequencies. The interesting is that the fundamental Fano line shape is produced in the present architectures. The enlarged views of Fano profiles in the insets of Figs. 2(c)–2(e) tell that the FR is pretty ideal, since the transmission is ultrasharp from zero to unity. The breaking of the lattice symmetry due to the cavity is responsible for the FR generation. The transmission spectra from Figs. 2(c)–2(e) also show that the zero transmission frequency point and the line width can be conveniently tuned through changing the coupling distance between the cavity and the WG.

Since the WG does not break the mirror symmetry of the cavity (along the vertical line crossing the cavity center) in Figs. 2(c)–2(e), the two cavity modes are still even and odd, respectively, according to their parities. These two cavity modes have different coupling strengths with the VESs, responsible for the FR. The wide transmission dip is attributed to the strong coupling between the odd cavity mode and the WG, while the Fano line shape is from the weak coupling of the even cavity mode with the WG. This can be observed from the field distributions in Figs. 2(f)–2(k) whose frequencies of the incident light beams correspond to the points of P1 to P6 in Fig. 2(c), respectively. Obviously, the field distributions for P1–P3 and P6 are mostly oddlike, while those for P4 and P5 are mostly evenlike. The magnetic field distributions for P4 and P5 points look nearly identical, because they both date from the even cavity mode. The fact that the coupling of the VESs with the odd cavity mode is stronger than that with the even one is owing to the different mode overlaps of the odd and even cavity modes with the VESs; see Figs. 2(f)–2(k). Consequently, the cavity mode strongly coupled with the WG serves as a bright one, while that weakly coupled with the WG serves as a dark one [83–85], for the architectures in Figs. 2(c)–2(e). Note that the parity of the cavity modes is not responsible for the FR, because such a type of optical architectures can also present the FR transmission even when the two cavity modes have no parity, which will be seen from Figs. 3. The factor responsible for the FR is the large difference between the coupling strengths of the two cavity modes with the WG. The two cavity modes concur to bring about the destructive and constructive interferences that create the Fano line shape transmission spectra, which

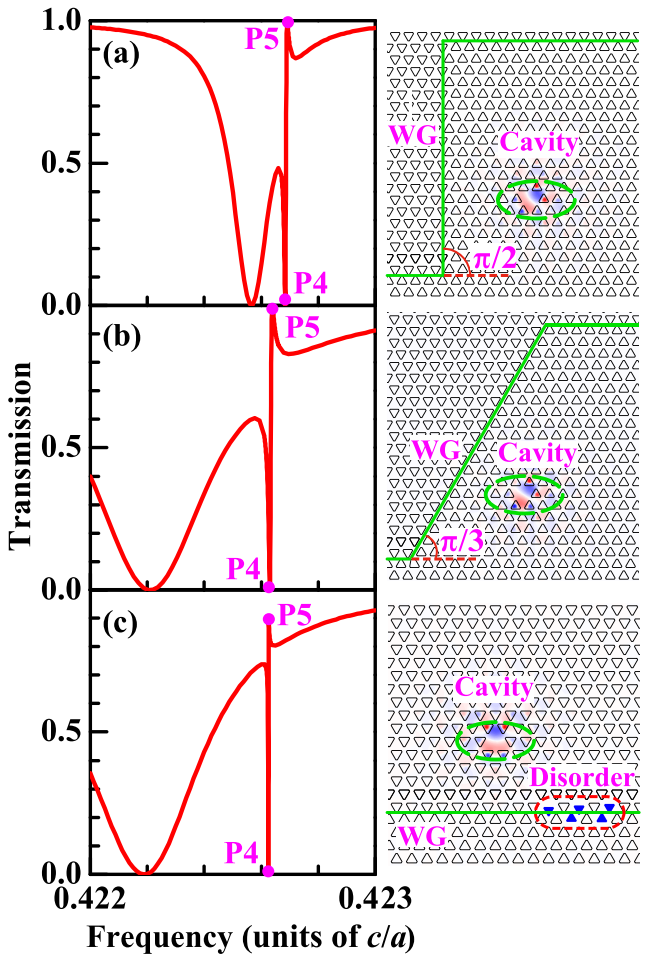

FIG. 3. (a, b) Transmission spectra of the valley-dependent edge states coupled with side cavity with different bending angles for the domain walls. (c) Transmission spectrum of the coupling system under disorder. The corresponding structures and field distributions for the P4/P5 are shown on the right side. The green lines indicate the domain walls and the green dashed ellipses indicate the position of the cavity. The red dashed oval denotes the disordered position.

will be confirmed by the δ-type coupling theory we build in Sec. IV.

The FR is always interesting in the realm of photonics [74,86–88] and has broad applicabilities in prominent optical devices, such as optical switches, low threshold lasers, filters with high quality factor, and ultrasensitive sensors [64,66,67,69]. The inherent characteristic of the ultrasharp asymmetric line shape is susceptible to the changes of the surrounding environment and geometry. This sensitivity stems from the change of modes to the environment and geometry. Especially, in nonrobust systems, such a sensitivity often makes it hard to achieve in experiments. Overcoming these unfavorable factors commonly requires advanced manufacturing techniques, associated with large costs. However, the topological modes are inherently stable against the changes of the surrounding environment and geometry due to the topological protection [89]. Thus, the robust Fano resonance can be obtained in the topological systems. The concept of the topological FR has been studied in one-dimensional periodic

acoustic system where the robustness is from the nontrivial Zak phase [90]. Differently, the robustness for the FR presented in Fig. 2 is from the nonzero valley Chern number, being another scheme. On the other hand, compared with the FR in the one-dimensional system, the two-dimensional optical architecture with easy fabrication in Fig. 2 can show more potentials in optics.

The robustness of the FR is numerically confirmed in Fig. 3 by introducing the bended WGs and the disorders. The two WGs with the bending angles of $\pi/2$ and $\pi/3$ are shown in Figs. 3(a) and 3(b), respectively, both which unequivocally tell that the Fano line shape is robust to the bended WGs. Note that the FR is also immune to other bending angles and multi-corner WGs [82], though they are not shown here. As one of the most common imperfections, the disorder is introduced by randomly perturbing the positions of some optical meta-atoms, see the red dashed oval in Fig. 3(c). Obviously, the corresponding spectrum demonstrates the existence of the FR. This is due to that the VESs are inherently stable against the changes of the surrounding environment and geometry. Though the disorder introduced in Fig. 3(c) cannot directly scatter the incident VESs back, it can disturb the local field distribution of the VESs and thereby, influence the coupling between the cavity mode and the VESs. This is responsible for the little deviation of the transmission peak from 1 in Fig. 3(c). Another feature is the perfect reflection, i.e., the zero transmission at the P2 or P4 point, referred to Fig. 2(c). Since it does not disappear when introducing the bended WGs and disorders, it is also robust against the impurities; see Fig. 3. Note that the perfect reflection is hard to be realized in those trivial waveguide-cavity coupled systems in the presence of these impurities. Since the shape and eigenfrequency of the cavity modes strongly depend on the geometry of the cavities [61], the geometry of the cavity can be taken as another way for tuning the transport of the VESs. Similarly, other local photonic modes near the cavity can also be introduced to tune the cavity modes and thereby, to tune the transport of the VESs, for example, vacancy disorders. In contrast to previous studies on high transmission in the crystal-symmetry-protected topological insulators, the transport tuning of the VESs by a side-coupled cavity is another interesting feature, reflected by the perfect reflection and the FR. The FR, not only against the impurities but also with ideal characteristics, has many merits to serve as high-performance optical devices.

The origin of the FR for other topological interfaces is also investigated, see the structures and field distributions in the right column of Fig. 3. The field distributions correspond to the P4 or P5 points, both of which are nearly identical, similar with that in Fig. 2. It has been shown that the factor responsible for the FR is the large difference between the coupling strengths of the two cavity modes with the WG, rather than the parity of the cavity modes. In Figs. 2(c)–2(e), the coupling strength between the even cavity mode and the WG is, by chance, far weaker than that between the odd cavity mode and the WG. This is due to that the WG is composed of the angle-to-angle interface, referred to those cases in Figs. 2(c)–2(e) and Fig. 3(c). If the topological WG is composed of the side-to-side interface, then one will find the odd cavity mode has the far weaker coupling strength with the WG and therefore, the field distributions for the P4 and P5 present the odd parities, see Fig. 3(b), different from those field distributions in Figs. 2(i), 2(j) and 3(c). For these two types of the WGs, the cavity modes hold parities, owing to the mirror symmetry of the whole optical structure along the line normal to the WG and crossing the cavity center, see Figs. 2(c)–2(e) and 3(b)–3(c) (neglecting those regions far away from the cavity). However, for the WG in Fig. 3(a), the original D_3 and mirror symmetries of the cavity are both broken. Therefore, the two cavity modes in this case not only are nondegenerate, but also do not hold parity. The mode shown in the right panel of Fig. 3(a) has the weaker coupling strength with the WG. The other cavity mode, naturally, has the stronger coupling strength, whose field distribution is not shown. To summarize, the FR stems from the different coupling strengths of the two cavity modes with the VESs, determined by the overlap between the cavity mode and the VESs. In addition, the robustness of the FR is from the nonzero C_V against the system imperfections.

To demonstrate the merits of the FR in the photonic valley Hall systems, the Fig. 4 shows the FR in one trivial WG-cavity coupled system and the influence of the bended waveguide and the disorders on it, similar with those done in Fig. 3. The trivial WG is composed of the line defect on which all the angle-cut triangle meta-atoms are replaced by the cylinder rods with the radius $r = 0.2a$, see Fig. 4. The valley Chern number across the line defect is zero, since the two sides of the interface are both the PVHI described in Fig. 1(a). The transmission spectrum for the straight trivial WG, see Fig. 4(a), is similar with those for the VES WGs discussed heretofore. However, the transmission line shape changes a lot, when different defects are introduced, for example, waveguide bending in Figs. 4(b) and 4(c) and disorder in Fig. 4(d). Accordingly, the FR line shape in a trivial WG-cavity coupled system can be easily ruined by the system imperfections, dating from the high sensitivity of the trivial WG states to the system imperfections. Comparing the results in Fig. 4 with those in Fig. 3, the robustness of the FR is indeed tied to the nontrivial feature of the WG states.

IV. δ-TYPE COUPLING THEORY

To uncover the coupling mechanism between the cavity modes and the VESs, a photonic transport theory is builded based on the quantum field method in this section. Here, only the structures given in Figs. 2(c)–2(e) are taken as examples. We start from the following field Hamiltonian,

$$\mathcal{H} = \mathcal{H}_W + \mathcal{H}_C + \mathcal{H}_I, \tag{3}$$

where $\mathcal{H}_W$, $\mathcal{H}_C$, and $\mathcal{H}_I$ are the Hamiltonians for the WG, cavity, and their coupling. The WG Hamiltonian $\mathcal{H}_W$ reads [91–93],

$$\mathcal{H}_W = \int dx[\hat{L}^\dagger(x)\hat{\omega}(i\partial_x)\hat{L}(x) + \hat{R}^\dagger(x)\hat{\omega}(-i\partial_x)\hat{R}(x)], \tag{4}$$

where $\hat{R}^\dagger(x)$ and $\hat{L}^\dagger(x)$ [$\hat{R}(x)$ and $\hat{L}(x)$] express the creation (annihilation) operators of rightward- and leftward-moving VESs at the coordinate of x, respectively. The VES dispersion is linearized with the form of $\hat{\omega}(\pm i\partial_x) = \omega_0 \pm i v_g \frac{\partial}{\partial x}$ with the corresponding intercept ω_0 and group velocity v_g. Since the two cavity modes have the parity in Figs. 2(c)–2(e), the cavity

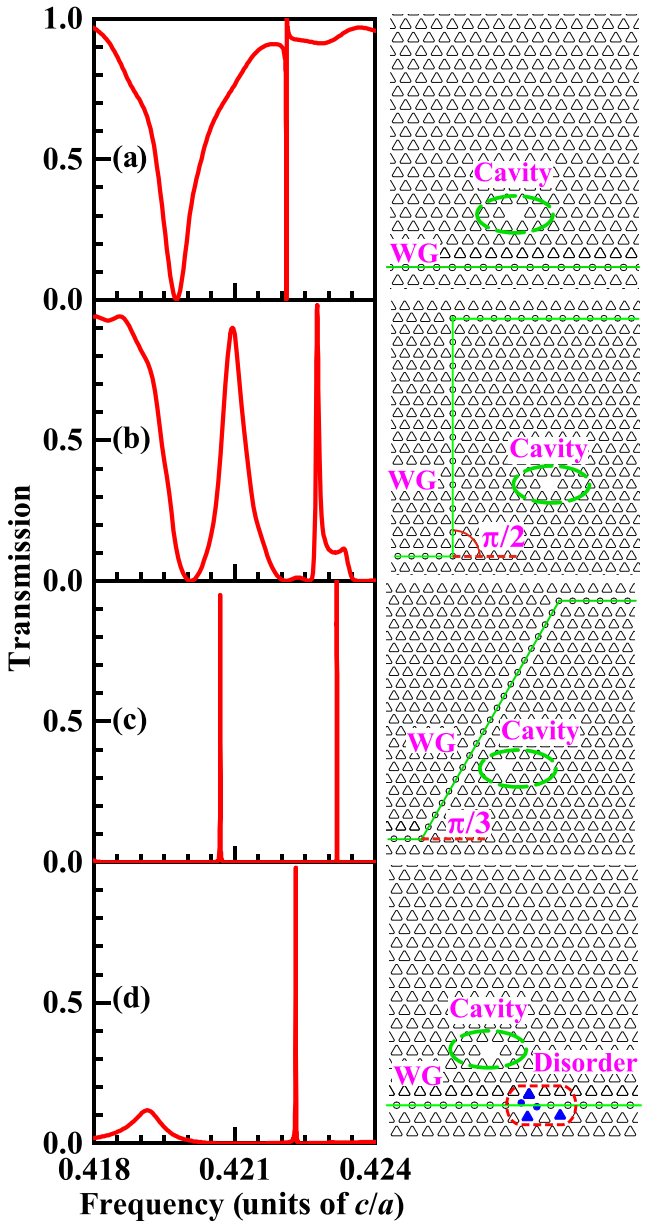

FIG. 4. (a–d) Transmission spectra of the trivial waveguide coupled with one side cavity. The wave guides are composed of the line defects, on which all the angle-cut triangle meta-atoms are replaced by the cylinder rods with the radius $r = 0.2a$. The photonic crystals on the two sides of the interface are both taken as the PVHI described in Fig. 1(a). In panel (a) the trivial waveguide is straight, in panels (b) and (c) the trivial waveguide is bended, and in panel (d) disorders are introduced along the trivial waveguide and denoted as blue dots.

Hamiltonian $\mathcal{H}_C$ can be written as

$$\mathcal{H}_C = \omega_O \hat{c}_O^\dagger \hat{c}_O + \omega_E \hat{c}_E^\dagger \hat{c}_E, \tag{5}$$

where $\hat{c}_O^\dagger$ and $\hat{c}_E^\dagger$ ($\hat{c}_O$ and $\hat{c}_E$) are the creation (annihilation) operators of the odd and even cavity modes with frequencies of ω_O and ω_E, respectively. Note that there is a small splitting between ω_O and ω_E due to the breaking of the cavity symmetry by the domain wall. According to the previous work [61], the coupling functions of the odd and even cavity modes with the VESs are also odd and even, respectively. Without loss of physics, we use the following Hamiltonian to describe the coupling between the two cavity modes and the VESs, i.e.,

$$\mathcal{H}_I = \int dx V_O[\delta(x+w) - \delta(x-w)][\hat{R}^\dagger(x) + \hat{L}^\dagger(x)]\hat{c}_O + \int dx V_E \delta(x)[\hat{R}^\dagger(x) + \hat{L}^\dagger(x)\hat{c}_E] + \text{H.c.}, \tag{6}$$

where V_O (V_E) is the coupling strength of the VESs with the odd (even) cavity mode. The width of w measures the extension of the odd coupling function along the WG direction, while the extension of the even coupling function is neglected. The cavity position is taken as the original point of coordinate x. The complex coupling functions, of course, can work also, such as the Gaussian function (even) and its first-order derivative (odd), but they outcome a too complex result to understand the underlying physics [61]. This is just the reason why the δ-type coupling functions are adopted in Eq. (6). Since they have caught the key information, i.e., the parity of the two cavity modes, they should be in agreement with the FR discussed above.

To find the system transmission, we use the following single-particle state,

$$|\Phi\rangle = (C_O c_O^\dagger + C_E c_E^\dagger)|\varnothing\rangle + \int dx[\mathcal{R}(x)\hat{R}^\dagger(x) + \mathcal{L}(x)\hat{L}^\dagger(x)]|\varnothing\rangle. \tag{7}$$

Here, $\mathcal{R}(x)$ and $\mathcal{L}(x)$ are the wave functions of the rightward- and leftward-moving VESs. C_O and C_E are the excitation amplitudes of the odd and even cavity modes. $|\varnothing\rangle$ represents the vacuum state with zero photons in the whole system. Substituting Eqs. (3) and (7) into the steady Schrödinger equation,

$$\mathcal{H}|\Phi\rangle = \omega|\Phi\rangle, \tag{8}$$

we arrive at a set of coupled equations for $\mathcal{R}(x)$, $\mathcal{L}(x)$, C_O, and C_E, i.e.,

$$\omega\mathcal{R}(x) = \hat{\omega}(-i\partial_x)\mathcal{R}(x) + V_O[\delta(x+w) - \delta(x-w)]C_O + V_E\delta(x)C_E, \tag{9a}$$

$$\omega\mathcal{L}(x) = \hat{\omega}(+i\partial_x)\mathcal{L}(x) + V_O[\delta(x+w) - \delta(x-w)]C_O + V_E\delta(x)C_E, \tag{9b}$$

$$\omega C_O = \omega_O C_O + V_O^*[\mathcal{R}(-w) + \mathcal{L}(-w) - \mathcal{R}(w) - \mathcal{L}(w)], \tag{9c}$$

$$\omega C_E = \omega_E C_E + V_E^*[\mathcal{R}(0) + \mathcal{L}(0)], \tag{9d}$$

with the frequency ω for the incident VES. Using the following wave functions $\mathcal{R}(x)$ and $\mathcal{L}(x)$,

$$\mathcal{R}(x) = \theta(-x-w)e^{ikx} + t_1\theta(-x)\theta(x+w)e^{ikx} + t_2\theta(x)\theta(-x+w)e^{ikx} + t\theta(x-w)e^{ikx}, \tag{10a}$$

$$\mathcal{L}(x) = r\theta(-x-w)e^{-ikx} + r_1\theta(-x)\theta(x+w)e^{-ikx} + r_2\theta(x)\theta(-x+w)e^{ikx}, \tag{10b}$$

where $\theta(x)$ is the step function. t and r are the total transmission and reflection coefficients, respectively. Substituting

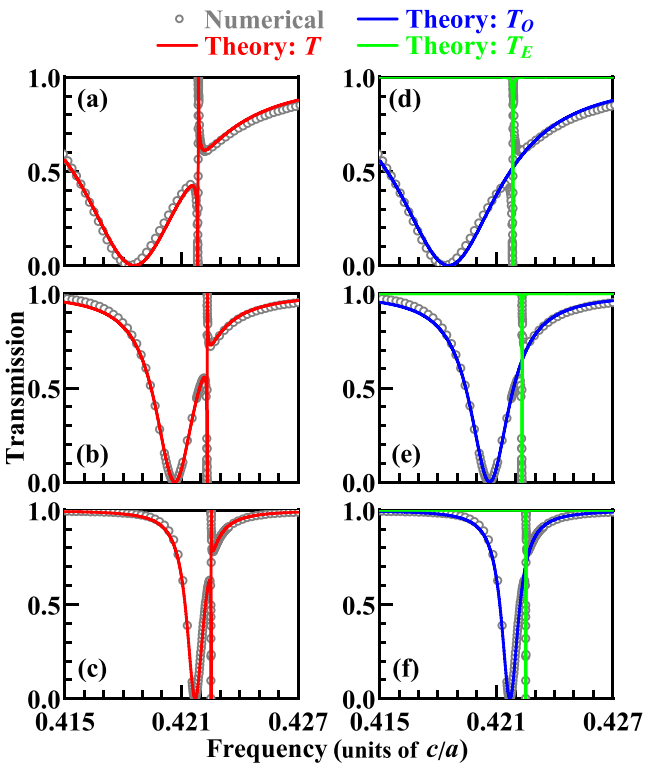

FIG. 5. (a–c) Theoretical fitting of the transmissivity T (red solid curves) with respect to the numerical data (gray circular dots). (d–f) Transmissivities T_O (blue curves) and T_E (green curves) corresponding to the transmissivity T in (a–c), respectively. The numerical data in panels (a–c) and (d–f) are identical with those in Figs. 2(c)–2(e), respectively.

Eq. (10) into Eq. (9) gives t as

$$t = 1 - i\frac{J_O[1-\cos(\phi)]}{[\omega-\omega_O+J_O\sin(\phi)]+iJ_O[1-\cos(\phi)]} - i\frac{J_E}{\omega-\omega_E+iJ_E}, \tag{11}$$

where $J_O = v_g^{-1}|V_O|^2$, $J_E = v_g^{-1}|V_E|^2$, and $\phi = 2kw$. The transmissivity reads $T = |t|^2$, which can well capture the FR of the system. The transmission coefficient can be divided into two types that account for the odd and even cavity modes. That is, the transmissivity $T_O = |t(J_E \equiv 0)|^2$ ($T_E = |t(J_O \equiv 0)|^2$) provides the transmission spectrum of the VESs just owing to the odd (even) cavity mode. As a result, the Fano line shape dates from the interference of these two types of the transmission.

This is confirmed by fitting the transmission spectra in Figs. 2(c)–2(e) with Eq. (11), whose results are demonstrated in Figs. 5(a)–5(c), respectively, and the corresponding fitting parameters of $(\omega_O, \omega_E, J_O, J_E, \phi)$ are listed in the Table I, which confirms that J_O is much larger than J_E, consistent with the discussion on Fig. 2. Note that the gray circular dots in Figs. 5(a)–5(c) are those replicas of the numerical data shown in Figs. 2(c)–2(e), respectively. Since the red fitted curves are in agreement with the numerical calculations, the key physics of the FR is well captured by the established theory, though it has a simple form. The FR dates from the interference of the two kinds of the transmissions that are controlled by the strongly-coupled cavity mode (odd parity) and the weakly-coupled one (even parity), respectively, which can be seen from Figs. 5(d)–5(f). The transmission spectra of T_O have a wide transmission dip, coinciding with the global behavior of the numerical data, while those of T_E have a far narrower transmission dip, coinciding with the FR positions. Their destructive and constructive interferences bring about the Fano line shape.

TABLE I. Fitting paramenters for Fig. 2.

	Fig. 2(c)	Fig. 2(d)	Fig. 2(e)
ω_O	$0.42146\frac{c}{a}$	$0.42205\frac{c}{a}$	$0.42223\frac{c}{a}$
ω_E	$0.42186\frac{c}{a}$	$0.42233\frac{c}{a}$	$0.42253\frac{c}{a}$
J_O	$2.91378\times10^{-3}\frac{c}{a}$	$1.39751\times10^{-3}\frac{c}{a}$	$5.23541\times10^{-4}\frac{c}{a}$
J_E	$1.47229\times10^{-5}\frac{c}{a}$	$7.02339\times10^{-6}\frac{c}{a}$	$3.34527\times10^{-6}\frac{c}{a}$
ϕ	0.52795π	0.46222π	0.49946π

The fitting parameters in Table I provide several important results. (i) The small frequency difference between the even and odd modes, i.e., $\omega_E - \omega_O$, roughly decreases with increasing the distance between the cavity and the WG, owing to the decrease of the breaking of the cavity symmetry D_3 by the domain wall. (ii) The coupling strengths of J_O and J_E also decrease with increasing the distance between the cavity and the WG. (iii) J_O is about 200 times larger than J_E, reflecting the odd cavity mode as a bright one with respect to the even cavity mode as a dark one for the angle-to-angle WGs in Figs. 2(c)–2(e). Here, it is also worthy pointing out that J_E is much larger than J_O for the side-to-side topological WG in Fig. 3(b). As a result, the FR is indeed not due to the mode parities. The factor responsible for the FR is the large difference between the coupling strengths of the two cavity modes with the WG. (iv) The phase of $\phi \approx 0.5\pi$ measures the extension of the odd coupling function along the WG direction, corresponding to $2w \approx 0.65a$ which is consistent with the field distribution in Figs. 2(g), 2(h), and 2(k). These qualitative analysis demonstrates that the topological FR originates from the interference of the two types of the transmission due to the coupling of the VESs with the two cavity modes. Since the δ-type coupling theory wonderfully catches the Fano line shape of the transmission spectra, it can provide a guidance for designing related topological optical devices. Moreover, such theory can also be used to describe the spatiotemporal evolution of the VESs, avoiding giant computing cost when simulating the VES transport in time domain with finite element method.

V. CONCLUSION

In summary, the photonic valley Hall insulators as a special case of the time reversal systems was used to reveal an inherent aspect that optical cavities with the resonance frequencies falling into the bulk band gap can completely destroy the robustness of the photonic edge state transport. This phenomenon and the related applications are both far less investigated in the field of the topological photonics. We demonstrated that an ideal Fano line shape for the

transmission spectra can be obtained when the valley edge states couple with a double-degenerate cavity, behaving as the sharply changing of the transmission from zero to one. The Fano resonance is well in agreement with the δ-type photonic transport theory we build. This theory reveals that the Fano resonance dates from the interference of the two transmissions that are controlled by the two cavity modes. These two cavity modes have large difference between their coupling strengths when they couple with the VESs. In addition, we also demonstrated that the Fano resonance in this photonic valley Hall system is robust against the imperfections, owing to the nonzero valley Chern number. On the contrary, the Fano resonance in a trivial waveguide can be easily ruined by the system imperfections, for examples, waveguide bending and disorders. Compared with the applications of the topological photonics in high transmission waveguides, delay lines, and topological lasers, this work may provide another realistic scheme to manipulate the valley transport and accordingly, possibly pave the way for a broad application of photonic valley Hall insulators in optical devices, such as switches and sensing.

ACKNOWLEDGMENTS

We thank Prof. Jian-hua Jiang for the useful discussion on the work. The authors also gratefully acknowledge financial support from the National Natural Science Foundation of China (Grants No. 12074037 and No. 11734003) and National Key R&D Program of China (Grant No. 2016YFA0300600).

[1] F. D. M. Haldane and S. Raghu, Phys. Rev. Lett. **100**, 013904 (2008).
[2] L. Lu, J. D. Joannopoulos, and M. Soljačić, Nat. Photon. **8**, 821 (2014).
[3] X.-C. Sun, C. He, X.-P. Liu, M.-H. Lu, S.-N. Zhu, and Y.-F. Chen, Prog. Quant. Electron. **55**, 52 (2017).
[4] Y. Wu, C. Li, X. Hu, Y. Ao, Y. Zhao, and Q. Gong, Adv. Opt. Mater. **5**, 1700357 (2017).
[5] A. B. Khanikaev and G. Shvets, Nat. Photon. **11**, 763 (2017).
[6] B.-Y. Xie, H.-F. Wang, X.-Y. Zhu, M.-H. Lu, Z. Wang, and Y.-F. Chen, Opt. Express **26**, 24531 (2018).
[7] T. Ozawa, H. M. Price, A. Amo, N. Goldman, M. Hafezi, L. Lu, M. C. Rechtsman, D. Schuster, J. Simon, O. Zilberberg, and I. Carusotto, Rev. Mod. Phys. **91**, 015006 (2019).
[8] M. S. Rider, S. J. Palmer, S. R. Pocock, X. Xiao, P. Arroyo Huidobro, and V. Giannini, J. Appl. Phys. **125**, 120901 (2019).
[9] Y. Ota, K. Takata, T. Ozawa, A. Amo, Z. Jia, B. Kante, M. Notomi, Y. Arakawa, and S. Iwamoto, Nanophotonics **9**, 547 (2020).
[10] K. v. Klitzing, G. Dorda, and M. Pepper, Phys. Rev. Lett **45**, 494 (1980).
[11] C. L. Kane and E. J. Mele, Phys. Rev. Lett **95**, 226801 (2005).
[12] B. A. Bernevig, T. L. Hughes, and S.-C. Zhang, Science **314**, 1757 (2006).
[13] J. E. Moore, Nature **464**, 194 (2010).
[14] L. Fu, Phys. Rev. Lett. **106**, 106802 (2011).
[15] Z. Wang, Y. D. Chong, J. D. Joannopoulos, and M. Soljačić, Phys. Rev. Lett. **100**, 013905 (2008).
[16] Z. Wang, Y. Chong, J. D. Joannopoulos, and M. Soljačić, Nature **461**, 772 (2009).
[17] A. B. Khanikaev, S. H. Mousavi, W.-K. Tse, M. Kargarian, A. H. MacDonald, and G. Shvets, Nat. Mater. **12**, 233 (2013).
[18] T. Ma, A. B. Khanikaev, S. H. Mousavi, and G. Shvets, Phys. Rev. Lett. **114**, 127401 (2015).
[19] L.-H. Wu and X. Hu, Phys. Rev. Lett. **114**, 223901 (2015).
[20] L. Xu, H.-X. Wang, Y.-D. Xu, H.-Y. Chen, and J.-H. Jiang, Opt. Express **24**, 18059 (2016).
[21] C. He, X.-C. Sun, X.-P. Liu, M.-H. Lu, Y. Chen, L. Feng, and Y.-F. Chen, Proc. Natl. Acad. Sci. USA **113**, 4924 (2016).
[22] X. Zhu, H.-X. Wang, C. Xu, Y. Lai, J.-H. Jiang, and S. John, Phys. Rev. B **97**, 085148 (2018).
[23] S. Barik, A. Karasahin, C. Flower, T. Cai, H. Miyake, W. DeGottardi, M. Hafezi, and E. Waks, Science **359**, 666 (2018).
[24] Y. Yang, Y. F. Xu, T. Xu, H.-X. Wang, J.-H. Jiang, X. Hu, and Z. H. Hang, Phys. Rev. Lett. **120**, 217401 (2018).
[25] S. Peng, N. J. Schilder, X. Ni, J. van de Groep, M. L. Brongersma, A. Alù, A. B. Khanikaev, H. A. Atwater, and A. Polman, Phys. Rev. Lett. **122**, 117401 (2019).
[26] L. Lu, L. Fu, J. D. Joannopoulos, and M. Soljačić, Nat. Photon. **7**, 294 (2013).
[27] L. Lu, Z. Wang, D. Ye, L. Ran, L. Fu, J. D. Joannopoulos, and M. Soljačić, Science **349**, 622 (2015).
[28] B. Yang, Q. Guo, B. Tremain, R. Liu, L. E. Barr, Q. Yan, W. Gao, H. Liu, Y. Xiang, J. Chen, C. Fang, A. Hibbins, L. Lu, and Z. Shuang, Science **359**, 1013 (2018).
[29] D. Wang, B. Yang, W. Gao, H. Jia, Q. Yang, X. Chen, M. Wei, C. Liu, M. Navarrocia, J. Han, W. Zhang, and S. Zhang, Nat. Phys. **15**, 1150 (2019).
[30] A. Cerjan, S. Huang, M. Wang, K. P. Chen, Y. Chong, and M. C. Rechtsman, Nat. Photon. **13**, 623 (2019).
[31] H. Jia, R. Zhang, W. Gao, Q. Guo, B. Yang, J. Hu, Y. Bi, Y. Xiang, C. Liu, and S. Zhang, Science **363**, 148 (2019).
[32] Y. Yang, W. Gao, L. Xia, H. Cheng, H. Jia, Y. Xiang, and S. Zhang, Phys. Rev. Lett. **123**, 033901 (2019).
[33] W. Ye, Y. Liu, J. Liu, S. A. R. Horsley, S. Wen, and S. Zhang, Light: Sci. Appl. **8**, 49 (2019).
[34] Z. Yin, F. Chen, K. Guo, F. Shen, K. Zhou, J. Gao, S. Liu, and Z. Guo, Opt. Express **27**, 512 (2019).
[35] B.-Y. Xie, H.-F. Wang, H.-X. Wang, X.-Y. Zhu, J.-H. Jiang, M.-H. Lu, and Y.-F. Chen, Phys. Rev. B **98**, 205147 (2018).
[36] S. Mittal, V. V. Orre, G. Zhu, M. A. Gorlach, A. Poddubny, and M. Hafezi, Nat. Photon. **13**, 692 (2019).
[37] A. El Hassan, F. K. Kunst, A. Moritz, G. Andler, E. J. Bergholtz, and M. Bourennane, Nat. Photon. **13**, 697 (2019).
[38] B.-Y. Xie, G.-X. Su, H.-F. Wang, H. Su, X.-P. Shen, P. Zhan, M.-H. Lu, Z.-L. Wang, and Y.-F. Chen, Phys. Rev. Lett. **122**, 233903 (2019).
[39] X.-D. Chen, W.-M. Deng, F.-L. Shi, F.-L. Zhao, M. Chen, and J.-W. Dong, Phys. Rev. Lett. **122**, 233902 (2019).
[40] Y. Ota, F. Liu, R. Katsumi, K. Watanabe, K. Wakabayashi, Y. Arakawa, and S. Iwamoto, Optica **6**, 786 (2019).
[41] T. Ma and G. Shvets, New J. Phys. **18**, 025012 (2016).

[42] Z. Gao, Z. Yang, F. Gao, H. Xue, Y. Yang, J. Dong, and B. Zhang, Phys. Rev. B **96**, 201402(R) (2017).
[43] X.-D. Chen, F.-L. Zhao, M. Chen, and J.-W. Dong, Phys. Rev. B **96**, 020202(R) (2017).
[44] J.-W. Dong, X.-D. Chen, H. Zhu, Y. Wang, and X. Zhang, Nat. Mater. **16**, 298 (2017).
[45] X.-D. Chen, F.-L. Shi, H. Liu, J.-C. Lu, W.-M. Deng, J.-Y. Dai, Q. Cheng, and J.-W. Dong, Phys. Rev. Appl. **10**, 044002 (2018).
[46] Y. Wu, X. Hu, and Q. Gong, Phys. Rev. Materials **2**, 122201(R) (2018).
[47] F. Gao, H. Xue, Z. Yang, K. Lai, Y. Yu, X. Lin, Y. Chong, G. Shvets, and B. Zhang, Nat. Phys. **14**, 140 (2018).
[48] Z. Xu, X. Kong, R. J. Davis, D. Bisharat, Y. Zhou, X. Yin, and D. F. Sievenpiper, Phys. Rev. Research **2**, 013209 (2020).
[49] T. Yamaguchi, Y. Ota, R. Katsumi, K. Watanabe, S. Ishida, A. Osada, Y. Arakawa, and S. Iwamoto, Appl. Phys. Express **12**, 062005 (2019).
[50] M. I. Shalaev, W. Walasik, A. Tsukernik, Y. Xu, and N. M. Litchinitser, Nat. Nanotech. **14**, 31 (2019).
[51] X.-T. He, E.-T. Liang, J.-J. Yuan, H.-Y. Qiu, X.-D. Chen, F.-L. Zhao, and J.-W. Dong, Nat. Commun. **10**, 872 (2019).
[52] X. Wu, Z. Li, J. Chen, X. Li, J. Tian, Y. Huang, S. Wang, W. Lu, B. Hou, C. T. Chan, and W. Wen, Adv. Opt. Mater. **7**, 1900872 (2019).
[53] H. Yoshimi, T. Yamaguchi, Y. Ota, Y. Arakawa, and S. Iwamoto, Opt. Lett. **45**, 2648 (2020).
[54] M. C. Rechtsman, J. M. Zeuner, Y. Plotnik, Y. Lumer, D. Podolsky, F. Dreisow, S. Nolte, M. Segev, and A. Szameit, Nature **496**, 196 (2013).
[55] W. Gao, M. Lawrence, B. Yang, F. Liu, F. Fang, B. Béri, J. Li, and S. Zhang, Phys. Rev. Lett. **114**, 037402 (2015).
[56] L. Lu, C. Fang, L. Fu, S. G. Johnson, J. D. Joannopoulos, and M. Soljačić, Nat. Phys. **12**, 337 (2016).
[57] Y. Yang, Z. Gao, H. Xue, L. Zhang, M. He, Z. Yang, R. Singh, Y. Chong, B. Zhang, and H. Chen, Nature **565**, 622 (2019).
[58] A. Lubatsch and R. Frank, Symmetry **11**, 1246 (2019).
[59] C. A. Valagiannopoulos, Progr. Electromag. Res. **71**, 277 (2007).
[60] A. Souslov, B. C. van Zuiden, D. Bartolo, and V. Vitelli, Nat. Phys. **13**, 1091 (2017).
[61] C.-Y. Ji, G.-B. Liu, Y. Zhang, B. Zou, and Y. Yao, Phys. Rev. A **99**, 043801 (2019).
[62] C.-Y. Ji, Y. Zhang, Y. Liao, X. Zhou, J.-H. Jiang, B. Zou, and Y. Yao, Phys. Rev. Research **2**, 013131 (2020).
[63] K. Nozaki, T. Tanabe, A. Shinya, S. Matsuo, T. Sato, H. Taniyama, and M. Notomi, Nat. Photon. **4**, 477 (2010).
[64] C. Wu, A. B. Khanikaev, R. Adato, N. Arju, A. A. Yanik, H. Altug, and G. Shvets, Nat. Mater. **11**, 69 (2012).
[65] T. Volz, A. Reinhard, M. Winger, A. Badolato, K. J. Hennessy, E. L. Hu, and A. Imamoğlu, Nat. Photon. **6**, 605 (2012).
[66] S.-L. Chua, Y. Chong, A. D. Stone, M. Soljačić, and J. Bravo-Abad, Opt. Express **19**, 1539 (2011).
[67] B. Zhen, S.-L. Chua, J. Lee, A. W. Rodriguez, X. Liang, S. G. Johnson, J. D. Joannopoulos, M. Soljačić, and O. Shapira, Proc. Natl. Acad. Sci. USA **110**, 13711 (2013).
[68] A. B. Khanikaev, C. Wu, and G. Shvets, Nanophotonics **2**, 247 (2013).
[69] L. Stern, M. Grajower, and U. Levy, Nat. Commun. **5**, 4865 (2014).
[70] K. P. Heeg, C. Ott, D. Schumacher, H.-C. Wille, R. Röhlsberger, T. Pfeifer, and J. Evers, Phys. Rev. Lett. **114**, 207401 (2015).
[71] K. Q. Le and J. Bai, J. Opt. Soc. Am. B **32**, 595 (2015).
[72] Z. Li, S. Zhang, L. Tong, P. Wang, B. Dong, and H. Xu, ACS Nano **8**, 701 (2013).
[73] Y. Zhao, C. Qian, K. Qiu, Y. Gao, and X. Xu, Opt. Express **23**, 9211 (2015).
[74] M. F. Limonov, M. V. Rybin, A. N. Poddubny, and Y. S. Kivshar, Nat. Photon. **11**, 543 (2017).
[75] Y. Wang, L. Liao, T. Hu, S. Luo, L. Wu, J. Wang, Z. Zhang, W. Xie, L. Sun, A. V. Kavokin, X. Shen, and Z. Chen, Phys. Rev. Lett. **118**, 063602 (2017).
[76] C. A. Valagiannopoulos, Prog. Electromagn. Res. **73**, 297 (2007).
[77] K. Lai, T. Ma, X. Bo, S. Anlage, and G. Shvets, Sci. Rep. **6**, 28453 (2016).
[78] Y. Kang, X. Ni, X. Cheng, A. B. Khanikaev, and A. Z. Genack, Nat. Commun. **9**, 3029 (2018).
[79] C. Hu, Z. Li, R. Tong, X. Wu, Z. Xia, L. Wang, S. Li, Y. Huang, S. Wang, B. Hou, C. T. Chan, and W. Wen, Phys. Rev. Lett. **121**, 024301 (2018).
[80] T. Fukui, Y. Hatsugai, and H. Suzuki, J. Phys. Soc. Japan **74**, 1674 (2005).
[81] Z. Zhu, X. Huang, J. Lu, M. Yan, F. Li, W. Deng, and Z. Liu, Phys. Rev. Appl. **12**, 024007 (2019).
[82] J. Lu, C. Qiu, L. Ye, X. Fan, M. Ke, F. Zhang, and Z. Liu, Nat. Phys. **13**, 369 (2017).
[83] S. Zhang, D. A. Genov, Y. Wang, M. Liu, and X. Zhang, Phys. Rev. Lett. **101**, 047401 (2008).
[84] B. S. Lukyanchuk, N. I. Zheludev, S. A. Maier, N. J. Halas, P. Nordlander, H. Giessen, and C. T. Chong, Nat. Mater. **9**, 707 (2010).
[85] E. Bochkova, S. Han, A. De Lustrac, R. Singh, S. N. Burokur, and A. Lupu, Opt. Lett. **43**, 3818 (2018).
[86] A. E. Miroshnichenko, S. Flach, and Y. S. Kivshar, Rev. Mod. Phys. **82**, 2257 (2010).
[87] S. A. Hassani Gangaraj, C. Valagiannopoulos, and F. Monticone, Phys. Rev. Reseasrch **2**, 023180 (2020).
[88] Z. Liu, Y. Xu, C.-Y. Ji, S. Chen, X. Li, X. Zhang, Y. Yao, and J. Li, Adv. Mater. **32**, 1907077 (2020).
[89] Q. Wang, H. Xue, B. Zhang, and Y. D. Chong, Phys. Rev. Lett. **124**, 243602 (2020).
[90] F. Zangeneh-Nejad and R. Fleury, Phys. Rev. Lett. **122**, 014301 (2019).
[91] J.-T. Shen and S. Fan, Phys. Rev. A **79**, 023838 (2009).
[92] W. Z. Jia and Z. D. Wang, Phys. Rev. A **88**, 063821 (2013).
[93] Q. Jiang, Q. Hu, B. Zou, and Y. Zhang, Phys. Rev. A **98**, 023830 (2018).